Azoulay, A.; García-Baldoví, A.; Albero-Sancho, J.; Azaria, N.; Tzadikov, J.; Tashakory, A.; Karjule, N.... (2023). Carbon-Phosphorus-Nitrogen Materials as Highly Thermally Stable Catalyst Supports for CO2 Hydrogenation to Methanol. ACS Applied Energy Materials. 6(1):439-446. https://doi.org/10.1021/acsaem.2c03410

Carbon-phosphorus-nitrogen materials as highly thermally stable catalyst supports for CO_2 hydrogenation to methanol

Adi Azoulay[a], Alberto Garcia Baldovi[b], Josep albero[b], Noa Azaria[c], Jonathan Tzadikov[a], Ayelet Tashakory[a], Neeta Karjule[a], Shmuel Hayun[c], Hermenegildo Garcia[b], and Menny Shalom*[a]

a. Department of Chemistry and Ilse Katz Institute for Nanoscale Science and Technology, Ben-Gurion University of the Negev, Beer-Sheva 8410501, Israel.

b. Instituto Universitario Mixto de Tecnología Química (UPV-CSIC), Universitat Politècnica de València, Avda. de los Narajos s/n, 46022, Valencia, Spain.

c. Department of Materials Engineering, Ben-Gurion University of the Negev, Beer-Sheva, Israel.

Introduction:

The development of sustainable and renewable carbon-neutral fuels and chemicals has been proposed as an appealing approach to mitigate CO_2 emissions.[1] The direct conversion of CO_2 into liquid fuels, such as methanol, through hydrogenation reactions using H_2 has attracted massive attention. Several pilot plants based on this approach have already been installed, with production capacities as high as 45,000 t/year.[2,3]

Methanol is among the top ten commodity chemicals (30×10^6 Mt/year)[4], and it is typically produced in the industry at high temperatures (200–300 ºC) and pressures (5–10 MPa) to achieve cost-effective conversion rates. Catalytic CO_2 hydrogenation (Equation 1) is considered impractical for industrial use, owing to the poor activity of the relevant catalysts. Moreover, competitive reactions occur in parallel at low temperatures and high pressures, particularly CO formation through the reverse water–gas shift reaction.[5–8] Therefore, highly efficient and robust catalysts are needed to increase the reaction rate and selectivity.

$$CO_2 + 3H_2 \rightarrow CH_3OH + H_2O;\ \Delta H^{o}_{298K} = -49.5\ (\mathrm{kJ\ mol^{-1}}) \qquad \text{Equation 1}$$

The most widely used catalyst for methanol synthesis via CO_2 hydrogenation has been $Cu/ZnO/Al_2O_3$.[9,10], although a large variety of Cu-based catalysts supported on different metal oxides

(e.g., Cu/ZnO/ZrO_2, Cu/CeO_2/TiO_2, and Pd-Cu/SiO_2), graphene-based materials, and MOFs have been investigated.[11–13]. Nevertheless, the catalytic performance of these Cu-based catalysts is still unsatisfactory because of the simultaneous formation of water (Eq. 1) as by-product promoting sintering and oxidation of the Cu active sites during the reaction, which leads to catalyst deactivation.[14,15] Besides, high Cu loadings also promote sintering, which limits the Cu content on the support.[16] Finally, CO is typically produced as a consequence of the reverse water–gas shift reaction occurring in parallel to the hydrogenation of CO_2 to methanol at low temperatures.[17] For these reasons, the design of new catalysts exhibiting high activity, selectivity, water tolerance, and stability is essential for the industrial development of CO_2 hydrogenation to methanol.

Over the last few years, metal-free materials have received considerable attention as catalyst supports owing to their favorable properties, such as high specific surface area, high mechanical strength, and strong metal–support interaction, which promote better metal dispersion and improve stability.[18] [19] [12] We recently reported the preparation of phosphorous-nitrogen-carbon materials with controllable elemental composition and structural, electronic, and thermal stability.[20] These materials exhibit remarkable stability up to 970 ºC in air and may be suitable for use as sustainable lightweight supports for metal-based catalysts.

The present study shows that Cu and Fe nanoparticles deposited on lightweight carbon-phosphorous-nitrogen materials exhibit excellent activity as catalysts for CO_2 hydrogenation to methanol, along with good stability. Our results show a high methanol production rate of 1.53 mol of MeOH $kgCat^{-1}$ h^{-1} at 250 ºC and under 20 bar, with notable stability of the catalyst and minor decay in the yield over the time. HRTEM analysis before and after the reaction revealed minor changes in the Cu and Fe nanoparticle morphology and oxidation state. This improved stability, which we attribute to a strong metal–support interaction, makes this catalyst support suitable to stand harsh conditions of the CO_2 hydrogenation to methanol.

Results and discussion:

Co crystals of MPA_x precursors (M stands for melamine, PA for phosphoric acid, and x = 2, 1, or 0.5 represents the molar ratio between melamine and phosphoric acid) were prepared by mixing melamine and phosphoric acid monomers in an aqueous solution for 1 h at 85 °C, then cooling the mixture to room temperature for another 1 h to complete the crystallization process. After filtration, the MPA_x crystals were washed several times with water and acetone to remove unreacted residues. Changes in the composition of the MPA*x* precursors alter their crystal structure, as shown in the X-ray diffraction (XRD) pattern (Figure 1a).[20] Fourier transform infrared (FTIR) measurements of the MPA_x precursors reveal the establishment of a hydrogen-bonded supramolecular framework (Figure 1b), as evidenced by the disappearance of the two sharp peaks at 3420, and 3470 cm^{-1} corresponding to the free amine groups in melamine. Inductively-coupled plasma optical emission spectroscopy (ICP-OES) and elemental analysis (EA) measurements of the MPA_x supramolecular precursors show that the elemental composition in the final crystal is controlled by the starting M:PA molar ratio (Figure 1c and Table S1). Indeed, a more elevated phosphorus content and lower carbon and nitrogen percentages in the MPA_x precursor were measured for the samples prepared with a lower M:PA molar ratio. The thermogravimetric analysis (TGA) curve of MPA_2 implies that when melamine is in excess, its self-condensation is favored at the expense of condensation with phosphoric acid, resulting in a significant mass loss at 290 °C (Figure 1d).[21] Meanwhile, the TGA profiles of both MPA_1 and $MPA_{0.5}$ show their superior thermal stability during calcination and higher mass yields of 23 and 26%, respectively. This lesser mass lose is probably due to an increased number of interactions between melamine and phosphoric acid, which disfavours melamine sublimation (Figures 1e, 1f).

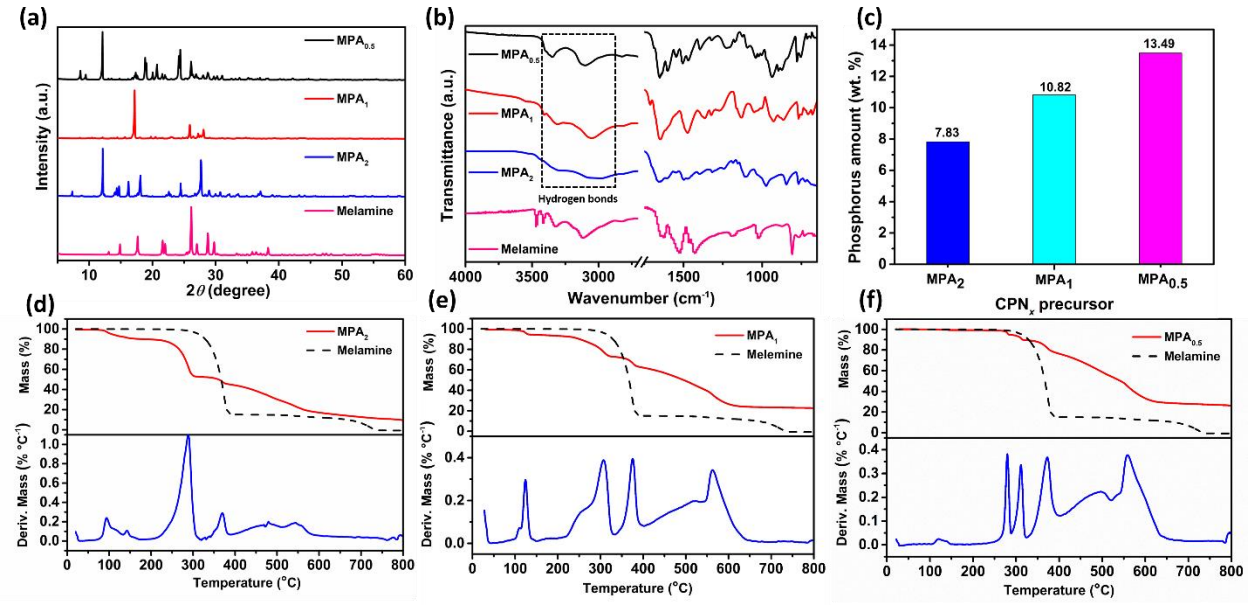

Figure 1. (a) XRD patterns and (b) FTIR spectra of MPA_x precursors and melamine. (c) Phosphorous concentrations (wt%) in MPA_x, provided by ICP-OES and their (d-e) TGA profiles under a N_2 environment.

Scanning electron microscopy (SEM) images of the MPA_x supramolecular precursors reveal smooth and ordered structures, where the initial M:PA molar ratio determines the shape of each precursor crystal (Figure 2a–c).

Carbon-phosphorus-nitrogen (CPN_x, where x is the initial M:PA molar ratio) materials were prepared by thermal treatment of MPA_x precursors at 800 °C for 4 h under a nitrogen environment to ensure full condensation and the formation of thermally stable P–N bonds within the structure (the complete synthetic procedure is illustrated in scheme 1). The well-defined size and shape of the precursor enable the transfer of their macrostructures to the final CPN_x materials, as shown in the SEM images (Figure 2d–f). This observation is in agreement with previous reports, which demonstrate the merit of using supramolecular crystalline materials as precursors to control the structure of the final materials.[20,22,23] The XRD patterns of the CPN_x display signals corresponding to amorphous structure, with a single broad diffraction peak located at 23.1° (Figure S1a). FTIR spectra confirmed the formation of a polyphosphazene network: the C–O–P stretching vibration is visible at 750 cm^{-1}, and the stretching

modes of phosphate groups, ν(P–O–P)[24] and ν(P=O),[25] and heptazine units, ν(C–N/C–N=C)[26] can be seen at 915, 1222, and 2162 cm $^{-1}$, respectively (Figure S1b).

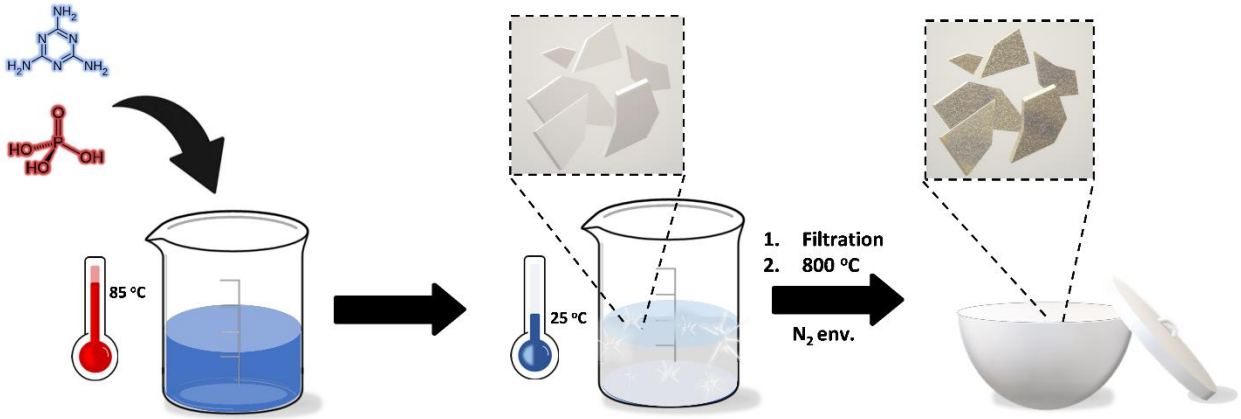

Scheme 1. Preparation of MPA_1 co-crystals, followed by calcination at 800 °C to form CPN_1.

The elemental composition of the CPN_x materials is directly related to the distribution of P, N, and C in the precursors; nevertheless, their P content values are close to each other (Figure S1c and Table S2). The CPN_x materials mainly contain phosphorus and nitrogen elements after calcination at 800 °C. In comparison with the elemental composition of the MPA_x precursors, the carbon content is low, owing to the formation of a thermodynamically favorable P–N network during the calcination process. X-ray photoelectron spectroscopy (XPS) P 2p spectra of CPN_x (Figure S2a) show two signals centered at 133.8–134.4 and 136.0–136.8 eV, the former corresponding to −N=P and −P−N species and the latter to oxidized phosphorus (PO_x).[27] The N 1s spectrum of CPN_1 reveals four peaks, at 397.5, 398.7, 399.7, and 401.0 eV, related to −N=P and −P−N species, pyridinic nitrogen group (C−N=C), neutral nitrogen (–NH–) and positively charged nitrogen (–NH^+–), respectively (Figure S2b).[28–30] These peaks indicating the formation of a polyphosphazene scaffold are observed in all CPN_x materials. C1s core-level spectra on the surface of CPN_x exhibit four peaks at 284.8, 286.4–286.6, 288.2–288.5, and 290.0–290.4 eV, assigned to sp^2 C-C, C−O, C=N−C, and O=C−O, respectively (Figure S2c).[20] O1s spectra confirm the presence of all the oxide species mentioned above (Figure S2d).

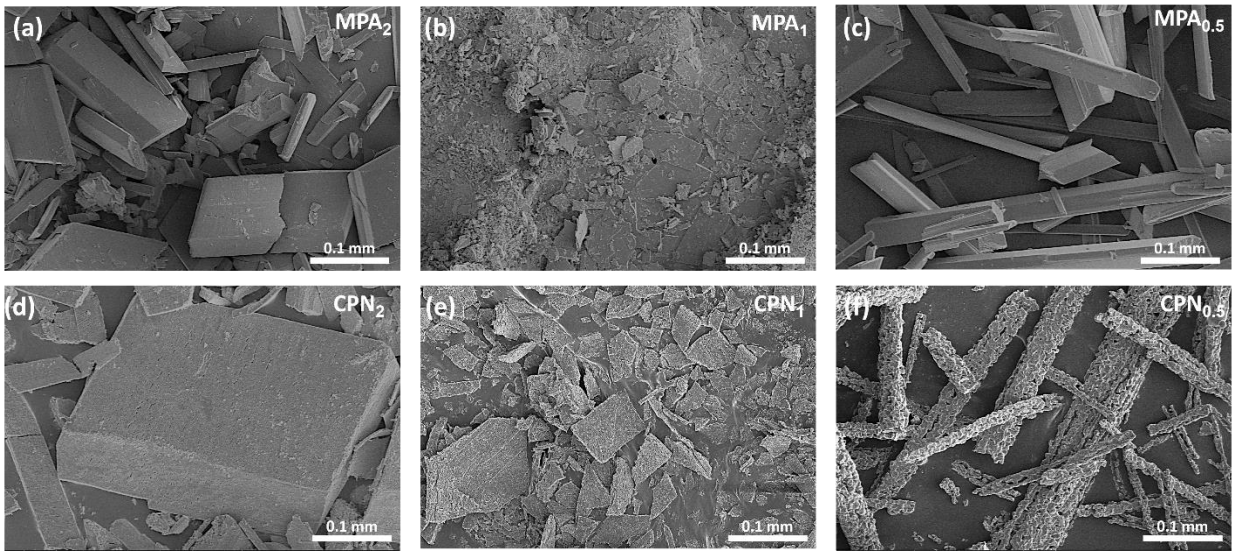

Figure 2. SEM images of (a–c) MPA_x co-crystals and (d–f) their corresponding products after calcination at 800 °C.

CO_2 full isotherms and N_2 sorption measurements of the CPNs show that they are made of mesoporous structures with considerable CO_2 capture capacity (Figure S3). CPN_2 shows the highest CO_2 uptake, 0.16 mmol g^{-1}, whereas CPN_1 and $CPN_{0.5}$ have slightly lower CO_2 capacities: 0.14 and 0.13 mmol g^{-1}, respectively. These values are similar to that reported for bulk polymerized ionic liquids (ca. 0.13 mmol g^{-1}), which are functional materials commonly used for CO_2 capture and separation.[31] In contrast with their CO_2 affinity, the CPN_x materials exhibit low specific surface areas as determined from N_2 sorption measurements (6.84 ± 0.06, 5.64 ± 0.20, and 3.77 ± 0.08 m^2 g^{-1} for CPN_2, CPN_1, and $CPN_{0.5}$, respectively), suggesting that their elemental composition and/or the presence of ultramicropores are the main factors behind their CO_2 adsorption capability (Table S3). The enhanced CO_2 uptake in CPN_2 could be related to its higher carbon content, which increases the surface polarity of the carbon-phosphorous-nitrogen-based material and thereby amplifies the uptake of CO_2.[32] Furthermore, CPN_2 displays a smaller BJH (Barrett-Joyner-Halenda) adsorption average pore width than CPN_1 and $CPN_{0.5}$, contributing to its superior CO_2 capture capacity.[33] Considering the low surface area of the CPNs, which reduces the adsorption uptake per contact area, these values of CO_2 adsorption are remarkably high. TGA studies of the CPN_x materials in air demonstrate their high thermal stability, a consequence of the large number of PN bonds within their structure (Figure S4). Although CPN_2 shows the highest

CO_2 capacity, it presents the lowest oxidation resistance, with a 10 % increase in material mass at 250 °C, which is likely due to the oxidation of surface carbon species. CPN_1 and $CPN_{0.5}$ undergo a mass increase of 2 and 6 % at the same temperature. These results highlight the good oxidation resistance of CPN_1 compared to the other CPNs, positioning it as the most suitable substrate for high-temperature catalysis, where self-oxidation plays a prominent role in catalyst deactivation.

We conducted ^{31}P and ^{13}C solid-state magic-angle spinning (MAS) nuclear magnetic resonance (NMR) experiments to elucidate the reaction pathway and analyze the CPN_1 material calcined at 800 °C (Figure S5 and figure S6). To help with the former, we synthesized three intermediates at different calcination temperatures; 350, 450, and 550 °C. The ^{31}P NMR spectrum of the MPA_1 supramolecular precursor shows three peaks from –1 to 4 ppm. According to the modeling we applied in our previous work, these peaks probably correspond to a phosphoric acid molecule attached to a deprotonated melamine unit.[20] The CPN_1 350 ^{31}P NMR signals are shifted to more negative values, from –20 to –30 ppm, revealing the formation of P–N bonds during the calcination procedure.[34] After thermal treatment at higher temperatures (450 and 550 °C), a unique broad signal was recorded, at a negative shift, indicating the amorphous nature of the sample, which probably consists of a mixture of different PN_xO_{4-x} species. The ^{31}P NMR spectrum of CPN_1 calcined at 800 °C shows three sharp peaks centered around 0, 10, and 23 ppm. These characteristic peaks are attributed to orthophosphate, pyrophosphate, and polyphosphate functional groups, respectively, and further corroborate the condensation of phosphoric acid and melamine molecules within the MPA_1 precursor into a fully polymerized structure.[35] The ^{13}C solid-state NMR spectrum of MPA_1 and those of the CPN_1 intermediates display two main signal groups around 158 and 164 ppm, corresponding to triazine carbon ($C–N_3$) and carbon attached to amine groups ($C–NH_x$), respectively. In congruence with the ICP results, no signal was detected in the ^{13}C NMR spectrum of CPN_1 800 ^{o}C, owing to the negligible carbon content of the sample.

High-resolution transmission electron microscope (HRTEM) images of CPN_1 indicate the formation of an amorphous structure (Figure 3a). High-angle annular dark-field (HAADF-STEM) reveals that the material consists of macroporous structures of different sizes throughout the sample, which agrees with the CO_2 adsorption isotherms (Figure 3b). Figures 3c–f also support the formation of a carbon-nitrogen-phosphorous scaffold, each element being homogeneously distributed throughout the sample.

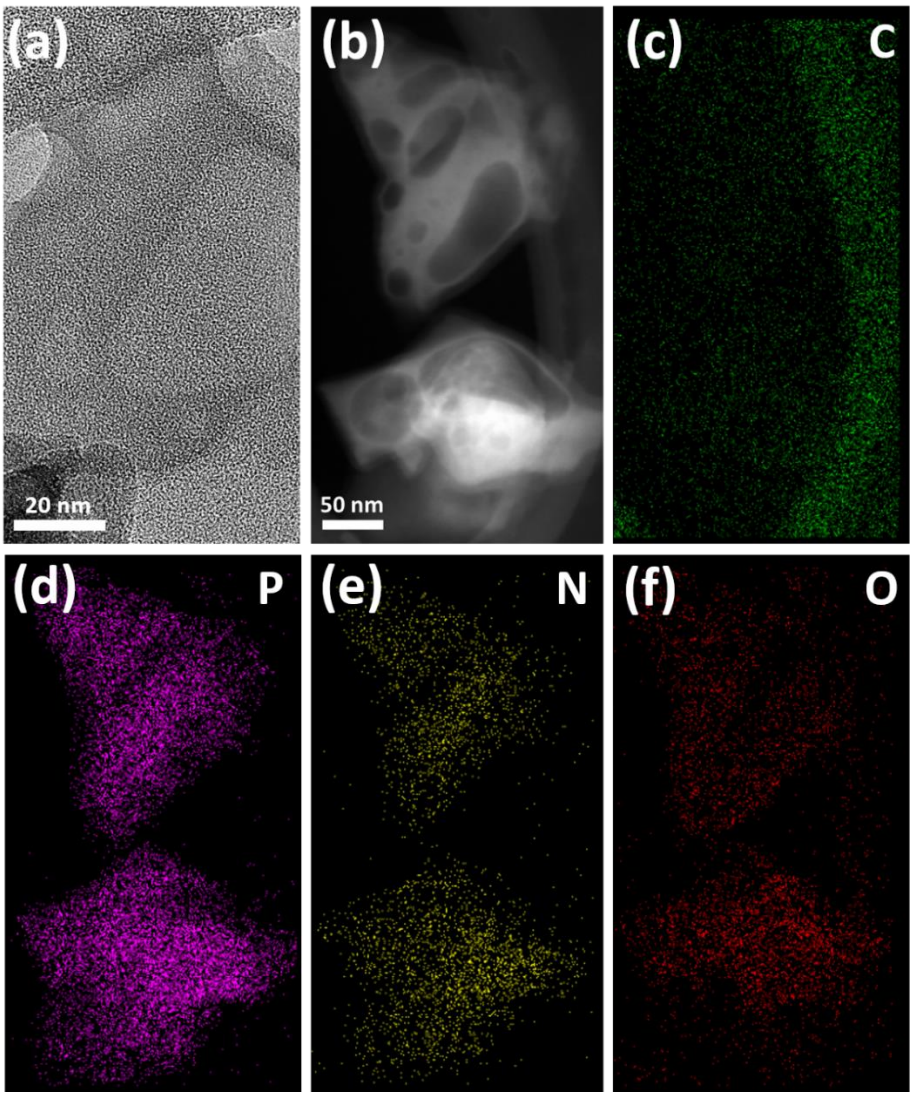

Figure 3. CPN_1 (a) TEM, (b) HAADF-STEM, and (c–f) EDS images.

To evaluate the activity and stability of the PNC_x materials as lightweight metal-free supports in catalytic reactions at high temperatures, we deposited Cu and Fe nanoparticles on CPN_1. While the

typical alloy in CO_2 hydrogenation to methanol is Cu-Zn alloy, the combination of Cu and Fe is much less explored. Then, we studied the catalytic activity of the resulting supported catalyst for CO_2 hydrogenation. We selected CPN_1 as a stable metal-free support on account of its superior resistance to oxidation at high temperatures, good CO_2 adsorption capacity, and small average pore width. A $CuFe/CPN_1$ catalyst was synthesized by wet impregnation of CPN_1 with a copper (II) nitrate aqueous solution to obtain a Cu concentration of 7.5 wt%, followed by thermal reduction under a H_2:N_2 (5:95, v/v) atmosphere to afford Cu^0/CPN_1, and subsequent impregnation of the reduced Cu/CPN_1 with an iron (III) nitrate nonahydrate solution to form 5 wt% of iron content followed by H_2:N_2 (5:95 v/v) reduction treatment. The resulting $CuFe/CPN_1$ catalyst was washed several times with water and acetone to remove unreacted metal salts.

The chemical states of $CuFe/CPN_1$ were determined via XPS measurements. The presence of a doublet at 933.3 and 952.7 eV in the Cu core-level spectrum shows the formation of CuO, indicating the spontaneous oxidation of Cu nanoparticles upon storage in air (Figure S7a). Another doublet at 936.1 and 955.5 eV, accompanied by satellite peaks at 943.0 and 962.8 eV, is assigned to $Cu(OH)_2$.[36] The Fe 2p electronic configuration is deconvoluted into three doublets, corresponding to FeO and Fe_2O_3 (FeO is associated with the doublet peak at 711.0 and 723.8 eV, Fe_2O_3 with the doublet at 713.4 and 726.3 and its satellite doublet at 717.0 and 728.8 eV).[37] with no evidence for the presence of metallic iron (Figure S7b). Overall, the XPS C 1s, N 1s, and P 2p spectra of CuFe/CPN1 show only a few changes after the addition of metal, namely, no amine (–NH–) group is detected in the N 1s spectrum and the peaks are shifted to higher values, probably a reflection of the charge transfer of the CPN_1 to the metal oxide on the sample surface (Figures S7 c–e). The O 1s XPS spectrum verifies the formation of metal oxides and other oxides species mentioned above (Figure S7f). The XRD pattern of $CuFe/CPN_1$ further confirms the formation of CuFe metallic sites on the CPN_1 support after the reduction treatment (Figure S8). The ICP data reveals a metal loading of 5.98 wt% Cu and 3.02 wt% Fe on CPN_1. We chose this metal composition to see if the current limitations of $Cu/ZnO/Al_2O_3$ in

terms of low activity and insufficient selectivity can be overcome by a different Cu alloying in a metal-free support. Precedents on the use of Cu-Fe combination for CO_2 hydrogenation to methanol are reported in the literature.[38,39]

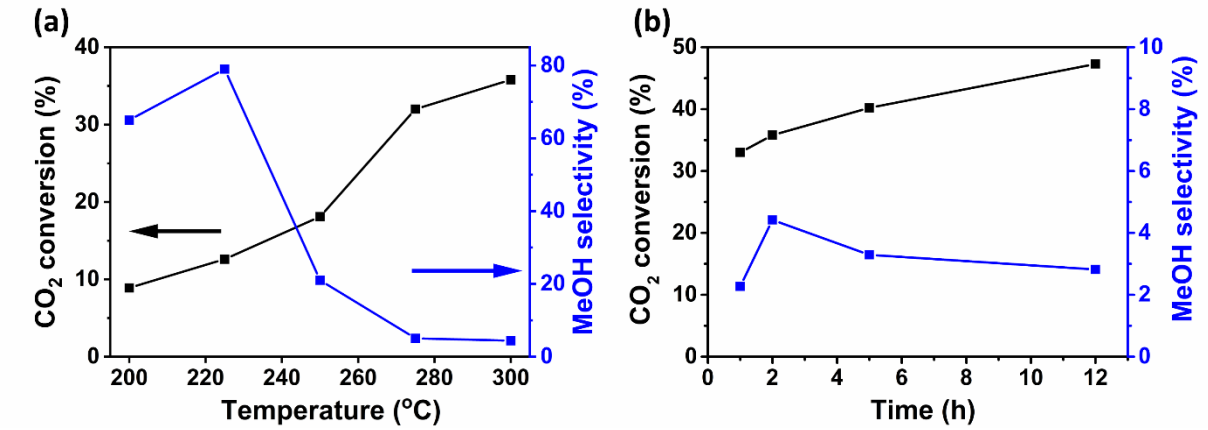

Figure 4. (a) CO_2 conversion and MeOH selectivity for CO_2 hydrogenation catalyzed by CuFe/CNP_1 for 2 h at different reaction temperatures. (b) Evolution of conversion and selectivity at a reaction temperature of 300 °C over 12 h. Reaction conditions: 20 bar, 15 mL/min CO_2, 3:1 v:v, H_2:CO_2, 100 mg catalyst.

Considering the presence of Cu and Fe oxide on the surface revealed by XPS, the catalysts were activated at 300 °C for 1 h under pure hydrogen flow before the reaction to reduce these surface metal-oxides species. The catalysts were then exposed to a flow of 15 mL/min of CO_2 and H_2 (3:1, v:v) at various temperatures in the range 200–300 °C with 20 °C increments. At each temperature the reactor was allowed to equilibrate for 1 h and then the composition of the reaction mixture was analyzed by gas chromatography in triplicate at 15 min interval. Differences in the three measurements were lesser than 10 %. The main reaction products, methanol, ethanol, and methane, were accompanied by lesser amounts of ethane and CO. The results of the activity test for CuFe/CPN_1 regarding CO_2 conversion and methanol selectivity are summarized in Figure 4a. As expected, CO_2 conversion increased with temperature, from 8.9% (at 200 °C) to 35.8% (at 300°C). In contrast, methanol selectivity exhibited the inverse trend. However, due to the higher CO_2 conversion, the CH_3OH production rate also increased

as a function of temperature, from 0.015 to 1.53 $mol_{CH_3OH} \cdot kg_{catalyst}^{-1} \cdot h^{-1}$ at reaction temperatures of 200 to 300 ºC, respectively. At 200 ºC, when CO_2 conversion was 9.3 %, the major product was methanol (65 %), accompanied by a rather notable percentage of ethanol (26 %), giving a remarkable combined alcohol selectivity over 90 %. The maximum methanol selectivity was achieved at 225 ºC (79 %) and a CO_2 conversion of 12.6 %. However, at 250 ºC, the main product was CH_4 (76%), and CH_3OH selectivity decreased abruptly to 21%. Further increasing the reaction temperature resulted in even lower MeOH selectivity, with methane as the major product. Interestingly, CO selectivity was consistently below 5% in the temperature range under study. Control experiments using CPN_1 in the absence of Cu and Fe revealed no catalytic activity under the same conditions, indicating that Cu and Fe are the active sites.

The catalytic data achieved with $CuFe/CNP_1$ compare favorably with data report in the literature. Table S4 in the supporting information provides a summary of reported data relevant to provide a valid assessment of the $CuFe/CNP_1$ performance. Thus, for instance, for Cu-Fe alloy supported on Al_2O_3 or Al_2O_3/CeO_2 no methanol formation was observed.[1, 2] Cu/Fe_2O_3 afforded at 230 ºC only 6.3 % methanol selectivity at a CO_2 conversion of 6.6 %.[3] The data presented in Figure 4 are similar, but still better, than those typically reported for the Cu-Zn alloys. As an example $Cu/ZnO/ZrO_2$ exhibits at 240 ºC a CO_2 conversion of 17.6 % with a 49 % methanol selectivity.[4] It is proposed that the catalytic performance of $CuFe/CNP_1$ is due to the activity of Cu-Fe alloy with a strong interaction with the CNP1 support as indicated by XPS binding energy.

Importantly, the $CuFe/CNP_1$ stability after extended use was confirmed by a catalytic test carried out at 300 ºC for 12 h (Figure 4 b). CO_2 conversion increased with time from 33 to 47.3%, and MeOH selectivity remained acceptably stablelduring the 12 h experiment. HRTEM images of the $CuFe/CPN_1$ before and after the reaction evidenced no substantial particle size or shape changes, emphasizing the remarkable stability of $CuFe/CNP_1$ under these harsh conditions (figure S9).

Conclusions:

The preparation of a stable, lightweight metal-free catalyst support that shows unprecedented oxidation resistance under the harsh conditions of the CO_2 hydrogenation to methanol has been reported. To do so, we designed carbon-phosphorus-nitrogen-based precursors with controllable elemental ratio, morphology and structural properties by using highly ordered supramolecular assemblies of melamine and phosphoric acid as precursors. Detailed structural analysis and CO_2 adsorption measurements reveal a correlation between the elemental composition of the CPNs and their CO_2 adsorption capability, which benefits CO_2 conversion to methanol. The unique surface features of CPNs also ensure the uniform dispersion of both Cu and Fe nanoparticles on CPN_1 and prevent sintering and the oxidation of the Cu active sites during the reaction. The new $CuFe/CNP_1$ catalyst exhibits a remarkable methanol production yield of 1.53 mol $kgCat.^{-1}$ h^{-1} at high temperature and pressure (250 °C, 20 bar). Moreover, thanks to the high thermal stability of the CPN_1 substrate and the strong metal–support interactions provided by its particular elemental composition, the supported $CuFe/CNP_1$ catalyst exhibits remarkable stability throughout a 12 h experiment under harsh conditions.

Experimental:

Materials

Melamine (99%, Alfa Aesar), Orthophosphoric acid (H_3PO_4 85 wt%, Bio-Lab Chemicals), 2-propanol (LOBA Chemie), nitric acid (HNO_3 67–69 wt%, trace metal grade, Fisher Chemical), copper(II) nitrate trihydrate (purum p.a., 98.0–103%, Sigma – Aldrich), Iron(III) nitrate nonahydrate (99+%, Acros Organics), and acetone (Bio-Lab AR grade) were used without further purification. Deionized water was purified using a Millipore Direct-Q3 water purification system (18.2 MΩ cm resistivity) and was used as a solvent in all experiments.

Synthetic procedures of carbon-phosphorus-nitrogen composites:

First, MPA_x crystalline precursors were prepared by dissolving 2 g of melamine in 150 mL of DI water, followed by the addition of certain amounts of phosphoric acid (85 wt% in H_2O) to obtain molar ratios of 1:2, 1:1, and 2:1 (melamine: H_3PO_4). The reaction mixtures were then placed on a pre-heated heating plate (85 °C) and mixed thoroughly. After 1h reaction time, each mixture was naturally cooled down to room temperature for another 1h, and filtered to extract the corresponding MPA_x supramolecular precursor. All MPA_x precursors were washed three times with water and then acetone.

The MPA_x precursors were transferred to lidded ceramic crucibles and calcined under N_2 atmosphere in a muffled furnace. The calcination process started by heating the precursors to 90 °C for 1h to remove

impurities. The temperature was then gradually increased to 800 °C at a constant heating ramp of 3 °C min^{-1}. Lastly, the precursors were kept at this temperature for 4h to complete the condensation procedure.

Cu and Fe deposition on CPN_1:

$CuFe/CNP_1$ catalyst was synthesized by dispersing 100 mg of CPN_1 in 20 mL MilliQ water using a tip sonicator (400W) for 0.5 h. An aqueous solution of copper(II) nitrate trihydrate was prepared by dissolving 7.5 wt% Cu in MilliQ water. The obtained solution was then added dropwise to the CPN_1 dispersion and kept under continuous stirring overnight at 60 °C to ensure water evaporation. After drying the resulted Cu(II)-CPN_1 at 100 °C for 3 h, it was thermally reduced to Cu^0-CPN_1 under H_2:N_2 (5:95, v/v) environment at 350 °C for 3 h (heating ramp of 10 °C min^{-1}). The reduced Cu/CNP_1 was impregnated with Fe(III) by using iron (III) nitrate nonahydrate aqueous solution containing 5wt% of Fe in the same manner. $CuFe/CNP_1$ was then washed with water and acetone to eliminate metallic salts residues.

Characterizations

XRD experiments were performed using a PANalytical's Empyrean diffractometer equipped with a position-sensitive detector X'Celerator. FTIR measurements were carried out on a Thermo Scientific Nicolet iS5 FTIR spectrometer equipped with a Si ATR.

Nitrogen adsorption–desorption isotherm measurements were conducted at –196 °C using an ASAP 2020 (Micrometrics, Norcross, GA) instrument. The surface areas were measured by the Brunauer–Emmett–Teller (BET) method. Ten-point adsorption isotherms of nitrogen were collected in the P P_0^{-1} relative pressure range (P_0 = saturation pressure) of 0.05–0.30 average; pore width and volume of pores were calculated using the Barrett-Joyner-Halenda (BJH) method. Prior to analysis, each sample was degassed under vacuum at 150 °C for 8 h. CO_2 full isotherm measurements were obtained using the same instrument at 25 °C. The CO_2 adsorption–desorption data were collected in the range of 0–800 mmHg (absolute pressure). Prior to analysis, each sample was degassed under vacuum at 150 °C for 8 h.

SEM images of MPA_x co-crystals and CPN_x materials after calcination were captured using a FEI Verios 460L high-resolution SEM equipped with a FEG 2S source and operated at 3.0 kV for imaging. All SEM samples were sputtered with gold (Au) before analysis. A JEOL JEM-2100F analytical TEM operated at 200 kV was used for HRTEM imaging, Scanning TEM (STEM) and EDS analysis. STEM was performed using a GATAN 806 HAADF (high-angle annular dark-field) STEM detector. EDS was performed using a JED-2300T energy dispersive X-ray spectrometer. The probe size during the analysis was set to 1 nm. The software JEOL Analytical Station (v. 3.8.0.21) was used to analyze the EDS data.

XPS was performed with a Thermo Fisher Scientific ESCALAB 250 using monochromated Kα X-rays (1486.6 eV). The data was collected with a scanning time of ca. 7 min over a 2θ range of 5° to 60° using Cu Kα radiation (λ = 1.54178 Å, 40 kV, 30 mA). Elemental analysis data for carbon, nitrogen, and hydrogen (CNH) was collected using a Thermo Scientific Flash Smart elemental analyzer OEA 2000. Samples for inductively-coupled plasma optical emission spectrometry (ICP OES) were prepared by dissolution in concentrated nitric acid in a PTFE-lined autoclave for 8 h at 180 °C and were then analyzed using a Spectro ARCOS ICP-OES, FHX22 multi-view plasma instrument (radial configuration). All MAS NMR experiments were carried out on a Bruker Avance III 500 MHz narrow-bore spectrometer, using a 4 mm double-resonance MAS probe at a spinning rate of 8 KHz. ^{13}C CP MAS experiments were carried out using a 2.5µs 1H 90°pulse, a 2 ms mixing time, and a 3 s recycle delay between acquisitions. ^{31}P CP MAS experiments were carried out using a 2.5µs ^{1}H 90° pulse, 3 ms mixing time and a 5 s recycle

delay between acquisitions. ^{31}P direct excitation experiments were carried out with use of a 3.860 μs 90° pulse and a recycle delay of 15s. CO_2 hydrogenation experiments were carried out in a pressurized stainless steel fixed bed reactor under continuous gas flow of a diluted CO_2:H_2 mixture (3:1, v:v). The evolved gases were analyzed using agas chromatography-mass spectrophotometer from Agilent (QP 6890 N) containing an HP5 column and EM detector (from 5 to 700 uam), and the products were quantified by gaschromatography using a Varian 3900 with FID detector and HP5 column, TRB-5, 30 m length and 0.25x0.25.

Acknowledgements:

The authors would like to thank Dr Natalya Froumin and Dr Keren Keinan-Adamsky for analytical XPS and solid-state NMR, respectively. This research was partly funded by the following: the Planning & Budgeting Committee/Israel Council for Higher Education (CHE) and Fuel Choice Initiative (Prime Minister Office of Israel), within the framework of "Israel National Research Center for Electrochemical Propulsion" (INREP); the Minerva Center No. 117873; the Spanish Ministerio de Econom´ıa y Competitividad (MAT2016-77608-C3-1-P, MAT2016-75883-C2-2- P); J. A. and H. G. also gratefully acknowledges Financial support from the Spanish Ministry of Economy and Competitiveness (Severo Ochoa SEV2016-0683 and RTI2018-89023-CO2- R1) and by the Generalitat Valenciana (Prometeo 2017-083). This project has received funding from the European Research Council (ERC) under the European Union's Horizon 2020 Research and Innovation Programme (grant agreement No. [849068]). NMR spectroscopic calculations were performed using HPC resources from GENCI-IDRIS (Grant 097535). The French Region Ile de France-SESAME program is acknowledged for □nancial support (700 MHz spectrometer).

References

[1] S.-T. Bai, G. De Smet, Y. Liao, R. Sun, C. Zhou, M. Beller, B. U. W. Maes, B. F. Sels, *Chem. Soc. Rev.* **2021**, *50*, 4259–4298.

[2] Chinese Academy of Sciences., "Thousand-tonne Scale Demonstration of Solar Fuel Synthesis Starts Operation in Lanzhou, China," can be found under https://english.cas.cn/newsroom/research_news/chem/202001/t20200113_229335.shtml, **2020**. (accessed June 16, 2022)

[3] "The North-C-Methanol project," can be found under https://northccuhub.eu/north-c-methanol/, **n.d.** (accessed June 16, 2022)

[4] R. Ladera, F. J. Pérez-Alonso, J. M. González-Carballo, M. Ojeda, S. Rojas, J. L. G. Fierro, *Appl. Catal. B Environ.* **2013**, *142–143*, 241–248.

[5] W.-H. Wang, Y. Himeda, J. T. Muckerman, G. F. Manbeck, E. Fujita, *Chem. Rev.* **2015**, *115*, 12936–12973.

[6] F. Studt, I. Sharafutdinov, F. Abild-Pedersen, C. F. Elkjær, J. S. Hummelshøj, S. Dahl, I. Chorkendorff, J. K. Nørskov, *Nat. Chem.* **2014**, *6*, 320–324.

[7] L. Kleinman, D. M. Bylander, *Phys. Rev. Lett.* **1982**, *48*, 1425–1428.

[8] J. Li, T. Du, Y. Li, H. Jia, Y. Wang, Y. Song, X. Fang, *J. Catal.* **2022**, *409*, 24–32.

[9] K. Li, J. G. Chen, *ACS Catal.* **2019**, *9*, 7840–7861.

[10] J. C. J. Bart, R. P. A. Sneeden, *Catal. Today* **1987**, *2*, 1–124.

[11] B. Rungtaweevoranit, J. Baek, J. R. Araujo, B. S. Archanjo, K. M. Choi, O. M. Yaghi, G. A. Somorjai, *Nano Lett.* **2016**, *16*, 7645–7649.

[12] T. Witoon, T. Numpilai, T. Phongamwong, W. Donphai, C. Boonyuen, C. Warakulwit, M. Chareonpanich, J. Limtrakul, *Chem. Eng. J.* **2018**, *334*, 1781–1791.

[13] S. Tada, K. Fujiwara, T. Yamamura, M. Nishijima, S. Uchida, R. Kikuchi, *Chem. Eng. J.* **2020**, *381*, 122750.

[14] H. Ahouari, A. Soualah, A. Le Valant, L. Pinard, P. Magnoux, Y. Pouilloux, *React. Kinet. Mech. Catal.* **2013**, *110*, 131–145.

[15] B. Liang, J. Ma, X. Su, C. Yang, H. Duan, H. Zhou, S. Deng, L. Li, Y. Huang, *Ind. Eng. Chem. Res.* **2019**, *58*, 9030–9037.

[16] A. Karelovic, P. Ruiz, *Catal. Sci. Technol.* **2015**, *5*, 869–881.

[17] S. Du, W. Tang, X. Lu, S. Wang, Y. Guo, P.-X. Gao, *Adv. Mater. Interfaces* **2018**, *5*, 1700730.

[18] I. Ud Din, M. S. Shaharun, D. Subbarao, A. Naeem, *J. Power Sources* **2015**, *274*, 619–628.

[19] Y. J. Fan, S. F. Wu, *J. CO2 Util.* **2016**, *16*, 150–156.

[20] A. Azoulay, J. Barrio, J. Tzadikov, M. Volokh, J. Albero, C. Gervais, P. Amo-Ochoa, H. García, F. Zamora, M. Shalom, *J. Mater. Chem. A* **2020**, *8*, 8752–8760.

[21] C. Duan, D. Yuan, Z. Yang, S. Li, L. Tao, Q. Wang, T. Wang, *Compos. Part A Appl. Sci. Manuf.* **2018**, *113*, 200–208.

[22] J. Barrio, S. Barzilai, N. Karjule, P. Amo-Ochoa, F. Zamora, M. Shalom, *Adv. Opt. Mater.* **2021**, *9*, 2100683.

[23] J. Barrio, L. Lin, P. Amo-Ochoa, J. Tzadikov, G. Peng, J. Sun, F. Zamora, X. Wang, M. Shalom, *Small* **2018**, *14*, 1800633.

[24] P. Stein, M. K. Dickson, D. M. Roundhill, *J. Am. Chem. Soc.* **1983**, *105*, 3489–3494.

[25] M. Mirzayi, M. H. Hekmatshoar, *Ionics (Kiel).* **2009**, *15*, 121–127.

[26] P. Gibot, F. Schnell, D. Spitzer, *Microporous Mesoporous Mater.* **2016**, *219*, 42–47.

[27] Y. Liu, P. Gao, T. Zhang, X. Zhu, M. Zhang, M. Chen, P. Du, G.-W. Wang, H. Ji, J. Yang, et al., *Angew. Chemie Int. Ed.* **2019**, *58*, 1479–1483.

[28] Y. Li, H. Zhang, Y. Jiang, M. Shi, M. Bawa, X. Wang, S. Zhu, *Fuel* **2019**, *241*, 861–869.

[29] L. Ge, C. Han, X. Xiao, L. Guo, Y. Li, *Mater. Res. Bull.* **2013**, *48*, 3919–3925.

[30] H. Ge, G. Qi, E.-T. Kang, K. G. Neoh, *Polymer (Guildf).* **1994**, *35*, 504–508.

[31] A. Wilke, J. Yuan, M. Antonietti, J. Weber, *ACS Macro Lett.* **2012**, *1*, 1028–1031.

[32] Y. Xia, Z. Tian, T. Heil, A. Meng, B. Cheng, S. Cao, J. Yu, M. Antonietti, *Joule* **2019**, *3*, 2792–2805.

[33] V. Zeleňák, M. Badaničová, D. Halamová, J. Čejka, A. Zukal, N. Murafa, G. Goerigk, *Chem. Eng.*

J. **2008**, *144*, 336–342.

[34] M. M. Velencoso, A. Battig, J. C. Markwart, B. Schartel, F. R. Wurm, *Angew. Chemie - Int. Ed.* **2018**, *57*, 10450–10467.

[35] P. Sannigrahi, E. Ingall, *Geochem. Trans.* **2005**, *6*, 52.

[36] S.-J. Chao, M.-H. Tsai, R.-P. Yu, L.-C. Hua, C.-C. Hu, C. Huang, *Environ. Sci. Water Res. Technol.* **2021**, *7*, 1666–1676.

[37] R. Zhang, Y. Li, T. Zhen, *RSC Adv.* **2014**, *4*, 52130–52139.

[38] S. Kiatphuengporn, M. Chareonpanich, J. Limtrakul, *Chem. Eng. J.* **2014**, *240*, 527–533.

[39] O. Tursunov, L. Kustov, A. Kustov, *Oil Gas Sci. Technol. – Rev. d'IFP Energies Nouv.* **2017**, *72*, 30.

1. L. Pastor-Pérez, F. Baibars, E. Le Sache, H. Arellano-García, S. Gu and T. R. Reina, *Journal of CO2 Utilization*, 2017, **21**, 423-428.
2. L. Yang, L. Pastor-Pérez, J. J. Villora-Pico, S. Gu, A. Sepúlveda-Escribano and T. R. Reina, *Applied Catalysis A: General*, 2020, **593**, 117442.
3. K. H. Lee and J. S. Lee, *Korean Journal of Chemical Engineering*, 1995, **12**, 460-465.
4. F. Arena, K. Barbera, G. Italiano, G. Bonura, L. Spadaro and F. Frusteri, *Journal of Catalysis*, 2007, **249**, 185-194.